MATERIALS.
TECHNOLOGIES.
DESIGN

УДК 620.178.3
P.A.C.S. 81.40.Np
DOI 10.54708/26587572_2026_822549

CRYSTALLOGRAPHY OF δ→γ PHASE TRANSFORMATION DURING LASER-POWDER-BED-FUSION OF 17-4 PH MARTENSITIC STEEL

Ivan Sergeyevich Zuiko [a], *Pavel Dmitriyevich Dolzhenko, Sergey Igorevich Borisov,*
Ivan Sergeyevich Nikitin, Aleksandr Andreyevich Kalinenko, Ksenia Sergeyevna Tuchina,
Elena Vladimirovna Kaliuzhnaya, Sergey Yuryevich Mironov

Belgorod National Research University, 85 Pobedy st., 308015 Belgorod, Russia
[a] zuiko_ivan@bsuedu.ru

ABSTRACT

This work was undertaken in order to shed some light on a poorly explored phase transformation of δ-ferrite to austenite (δ→γ) in steels. To this end, electron backscatter diffraction (EBSD) was employed to characterize the microstructure fabricated by laser powder bed fusion (L-PBF) of 17-4 PH martensitic steel. It was found that the phase transformation involved two different mechanisms, i.e., the displacive and diffusion-driven ones. The orientation relationship between the δ-ferrite and austenite spanned a wide range between the “classical” Kurdjumov–Sachs and Nishiyama–Wassermann relationships. Notably, the phase transformation was governed by a strict selection of crystallographic variants with a distinct preference for twin-related variants.

KEYWORDS

Phase transformations; martensitic steel; laser powder bed fusion (L-PBF); electron backscatter diffraction (EBSD).

КРИСТАЛЛОГРАФИЯ ФАЗОВОГО ПРЕВРАЩЕНИЯ δ→γ ПРИ ЛАЗЕРНОМ СПЛАВЛЕНИИ В ПОРОШКОВОМ СЛОЕ МАРТЕНСИТНОЙ СТАЛИ 17-4 PH

Иван Сергеевич Зуйко [a], *Павел Дмитриевич Долженко, Сергей Игоревич Борисов,*
Иван Сергеевич Никитин, Александр Андреевич Калиненко, Ксения Сергеевна Тучина,
Елена Владимировна Калюжная, Сергей Юрьевич Миронов

Белгородский государственный национальный исследовательский университет, Россия, 308015 Белгород, ул. Победы, 85
[a] zuiko_ivan@bsuedu.ru

АННОТАЦИЯ

Настоящая работа посвящена исследованию малоизученного фазового превращения δ-феррита в аустенит (δ→γ) в сталях. С этой целью метод дифракции обратно рассеянных электронов (EBSD) был применен для исследования микроструктуры, сформированной в процессе лазерного плавления в слое (L-PBF метод) мартенситно-стареющей стали 17-4 PH. Установлено, что фазовое превращение протекает по двум различным механизмам: сдвиговому и диффузионному. Ориентационные соотношения между δ-ферритом и аустенитом варьировались в широком диапазоне между классическими соотношениями Курдюмова–Закса и Нишиямы–Вассермана. Важно отметить, что превращение сопровождалось строгим отбором кристаллографических вариантов с явным предпочтением в пользу двойниковых вариантов.

КЛЮЧЕВЫЕ СЛОВА

Фазовые превращения; мартенситная сталь; селективное лазерное плавление; дифракция обратно рассеянных электронов.

Introduction

Given the enormous industrial significance of martensitic transformations in steels, these have been extensively investigated for over more than a century. Accordingly, this phenomenon is currently among the best-studied ones in materials science. In contrast, the transformation of δ-ferrite to austenite (δ→γ hereafter) has attracted much less attention so far. This was primarily due to the substantially lower practical importance of this process in conventional metalworking. An additional issue is also the high-temperature nature of this transformation, which challenges its detailed examination.

However, the recent invention of additive technologies has changed not only the fundamental concept of the manufacturing process but also the underlying metallurgical phenomena. Specifically, due to the unique nature of the laser powder bed fusion (L-PBF) technique, the additive products from martensitic steels often contain a significant fraction of δ-ferrite and austenite [e.g., 1, 2]. Accordingly, the δ→γ phase transformation may exert a significant influence on the service properties of the L-PBF'ed steels. Therefore, it becomes of particular interest.

A survey of the available scientific literature showed that the current knowledge on the δ→γ phase transformation is limited. Particularly, it is believed that the austenitic phase preferentially nucleates at the ferrite grain boundaries [3–5] and then propagates into the grain interior [5, 6]. The phase transformation is governed by the displacive mechanism [7, 8], but it may also be assisted by the diffusion-driven processes [9]. There is a scattering in the literature regarding the orientation relationship between the δ-ferrite and austenite. Often, the "classical" Kurdjumov–Sachs (K-S) relation is reported [3, 8, 10–12]. In some cases, however, the Nishiyama–Wasserman (N-W) [7] or even "mixed" orientation relations [4, 6, 9, 13] were also found.

Despite the above-mentioned works having provided valuable insight into the δ→γ transformation, it is believed that crystallographic aspects of this phenomenon are far from clear. The present study was undertaken in order to contribute to this issue. Considering the particular importance of this phenomenon in the field of additive manufacturing, it was studied in the L-PBF'ed 17-4 PH martensitic steel. Moreover, this technology provides an excellent opportunity to investigate this phase transformation directly.

1. Experimental

The program material used in this work was an atomized powder of commercial 17-4 PH martensitic steel. The nominal chemical composition of this steel is shown in Table 1. The material was produced by 3D Systems Inc. using the nitrogen-gas atomization technique. In the supplied material, the powder particles had a nearly spherical morphology and often contained satellites. The particle size ranged from 1.4 to 53.2 mm, with a mean volume diameter being 13.5 mm. The percentile diameters were $D_{10} \approx 4.2$ μm, $D_{50} \approx 11.5$ μm, and $D_{90} \approx 25.8$ μm.

Table 1. Nominal chemical composition of 17-4 PH martensitic steel (wt.%)

Таблица 1. Номинальный химический состав мартенситно-стареющей стали 17-4 PH (мас. %)

Fe	Cr	Ni	Cu	Mn	Si	Ta + Nb	C	P	S
Balance	15.0–17.5	3.0–5.0	3.0–5.0	≤1.0	≤1.0	0.15–0.45	≤0.07	≤0.04	≤0.03

The L-PBF process was performed on a ProX DMD 200 machine (3D Systems) under the manufacturer-recommended conditions, i.e., a laser power of 240 W, a laser scanning speed of 2500 mm/s, a hatch distance of 50 μm, and a layer thickness of 30 μm (the volumetric energy density of 64 J/mm^3). A simple parallel scan strategy was employed with the laser scan direction rotated by 90° between successive layers. A typical L-PBF geometry was adopted in this work, i.e., the building direction (BD), the motion direction of the powder roller (RD), and the transverse direction (TD). A cuboidal-shaped sample with dimensions of 10×10×20 mm^3 (RD×TD×BD) was built in a nitrogen atmosphere.

For microstructural observations, the built sample was sectioned in half along the building direction, mounted into a conductive resin, and mechanically polished using standard metallographic procedures. A final surface finish was achieved using ≈24 h vibratory polishing with an OP-S colloidal silica suspension.

The microstructural examinations were conducted using the electron backscatter diffraction (EBSD) technique. EBSD analysis was performed employing an FEI Quanta 600 field-emission-gun scanning electron microscope (FEG-SEM) equipped with TSL OIM™ software and operated at an accelerated voltage of 20 kV. Given the difficulty of discriminating ferrite from martensite in EBSD, these two phases were indexed as the generic body-centered phase; accordingly, the austenite was indexed as the generic face-centered cubic phase. To provide both a necessary spatial resolution and sufficient sampling statistics, an intermediate EBSD scan step size of 0.2 μm was applied. To enhance the reliability of EBSD data, the fine grains comprising two or one pixel were automatically "cleaned" from the acquired EBSD map using the standard grain-dilation option of EBSD software. To eliminate spurious boundaries caused by orientation noise, a lower limit boundary misorientation cut-off of 2° was applied.

2. Results and Discussion

Preliminary analysis. The typical EBSD image-quality[1] (IQ) map taken from the built sample is shown in Fig. 1. In Fig. 1, *a*, the austenitic phase is highlighted with red.

Despite the L-PBF process being conducted under the manufacturer-recommended regime, a measurable portion of volumetric defects was found within the additive material. A typical example of the lack-of-fusion defects is indicated by the arrow in Fig. 1, *a*.

In the line with the scientific literature [e.g., 1, 2], a more or less distinct "fish scale" structure was revealed (Fig. 1, *a*). It is often believed that such a mesoscale structure is intrinsic to the L-PBF process and arises from the highly localized nature of the melting-to-solidification sequence. Remarkably, the typical breadth of the local molten pools was close to ~100 μm, i.e., it was comparable with a laser beam diameter applied in the present study (≈78 μm). It is also important to emphasize that the characteristic depth of the pools significantly exceeded the nominal thickness of the powder layer, i.e., 30 μm (Fig. 1, *a*). This observation suggested that the additive material experienced several melting-to-solidification cycles during the L-PBF process.

---

[1] In TSL OIM software, the image quality (IQ) index characterizes the sharpness of the Kikuchi bands in a digitized diffraction pattern. The grayscale IQ maps are often similar to the corresponding optical (or scanning-electron-microscopy) images of a microstructure. Accordingly, those can be simple for comparison with conventional metallography.

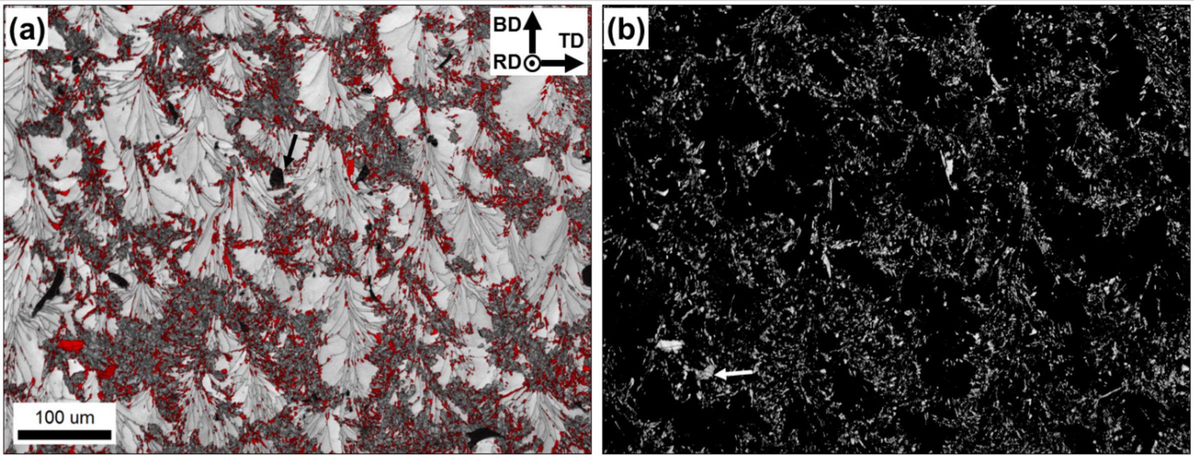

Fig. 1. EBSD image-quality map of produced microstructure:
a – entire map and b – austenite map. The common reference frame for the figures is given in the top right corner of (*a*); BD, RD, and TD define the building direction, the motion direction of the powder roller, and the transverse direction, respectively. In (*a*), austenitic phase is highlighted with red; arrow exemplifies a lack of fusion defect. In (*b*), arrow exemplifies an austenite particle with relatively high IQ index, which presumably originated from a recrystallization mechanism

Рис. 1. Карта качества изображения (IQ) EBSD сформированной микроструктуры:
а – общая карта и b – карта аустенита. Общая система координат для рисунков приведена в правом нижнем углу (*а*); BD, RD и TD обозначают направление выращивания, направление движения порошкового ролика и поперечное направление соответственно. На (*а*) аустенитная фаза выделена красным цветом; стрелкой показан пример дефекта несплавления. На (*b*) стрелкой показана частица аустенита с относительно высоким индексом IQ, которая, предположительно, образовалась по механизму рекристаллизации

Another important characteristic of the evolved microstructure was the fairly inhomogeneous character of its spatial distribution (Fig. 1, *a*). Specifically, the central part of the pools was typically occupied by the comparatively coarse columnar-shaped grains with a relatively high IQ index, which presumably represented δ-ferrite. The measured volume fraction of this phase was ≈57%.

On the other hand, the fine-grained austenite/martensite structure tended to cluster near the pool borders, preferentially along the laser tracks or at the pool triple joints. Moreover, the local austenite “islands” were also sporadically revealed along the δ-ferrite grain boundaries within the pools. The volume fraction of the austenitic phase was measured to be ≈17%.

Thus, in accordance with expectations, the produced microstructure was feasible for investigation of the δ→γ transformation. The relatively high content of both these metastable phases within the additive material was likely attributable to the extremely high cooling rate, which is intrinsic to the L-PBF process (~10^6 K/s).

To provide a preliminary insight into the phase transformation, the IQ map of the evolved austenitic phase was examined, as shown in Fig. 1, *b*. It is seen that the austenite particles typically exhibited a relatively dark IQ contrast (which implied an increased density of defects) and a lath-shaped morphology. From these observations, it can be inferred that the phase transformation was likely governed by the displacive mechanism, in a good agreement with the scientific literature [7, 8]. On the other hand, a minor fraction of the relatively coarse austenite particles with a bright IQ contrast was also found (an example is arrowed in Fig. 1, *b*). This finding may indicate that the diffusion processes also contributed to the δ→γ phase transformation, which was also in accordance with some references [9].

Orientation relationship. To evaluate a possible orientation relationship between austenite and δ-ferrite, the local orientations between the austenitic particles and the neighboring δ-ferrite matrix were compared, as exemplified in Fig. 2. Assuming either the Kurjumov–Sachs (K-S) $\{110\}_\delta$ // $\{111\}_\gamma$, $<111>_\delta$ // $<110>_\gamma$ or Nishiyama–Wasserman (N-W) $\{110\}_\delta$ // $\{111\}_\gamma$, $<110>_\delta$ // $<112>_\gamma$ relations between the phases, the appropriate pole figures were compared (Fig. 2, *a, b*). For clarity, crystallographic directions in the austenite that are close to the δ-ferrite were circled.

It was found that the δ/γ relationship lay between the classical K-S and N-W ones. The revealed uncertainty was attributed to the limited accuracy of the EBSD technique in the determination of orientation axes (≈5°, according to Wilkinson [14]). Given the relatively small difference between the K-S and N-W relationships, it is challenging to distinguish between them without bias when using EBSD.

To provide a more statistically reliable insight into the orientation relationship between the phases, misorientations across the phase boundaries were measured using the standard options of EBSD software. Specifically, a particular orientation relationship can be expressed in terms of a particular misorientation [e.g., 15, 16]. Those were systematically measured and summarized as misorientation-angle and misorientation-axis distributions in Fig. 3, *a, b*, respectively. For clarity, the particular orientation relationships were indicated in the distributions.

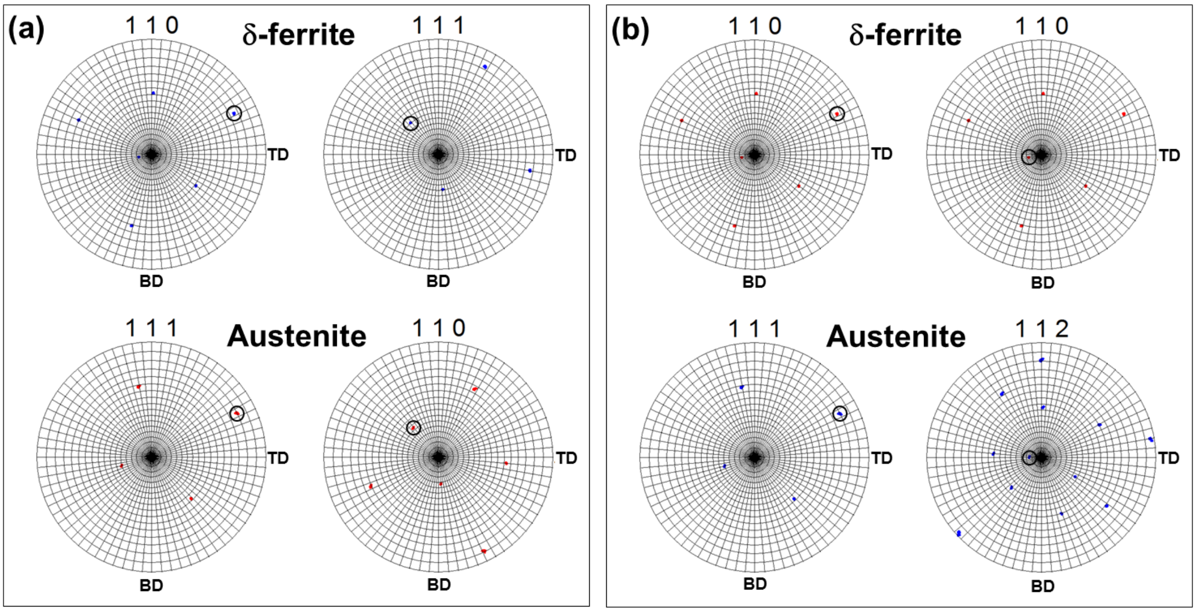

Fig. 2. Pole figures showing a typical orientation relationship between δ-ferrite and austenite:
a – Kurdjumov–Sachs (K-S) relation and b – Nishiyama–Wasserman (N-W) relation.
In the pole figures, the closest related directions in δ-ferrite and austenite are circled.
BD and TD define the building direction and the transverse direction, respectively

Рис. 2. Полюсные фигуры, демонстрирующие типичное ориентационное соотношение между δ-ферритом и аустенитом:
а – соотношение Курдюмова–Закса (К-З) и b – соотношение Нишиямы–Вассермана (Н-В).
На полюсных фигурах кружками обведены наиболее близкие кристаллографические направления в δ-феррите и аустените. BD и TD обозначают направление выращивания и поперечное направление соответственно

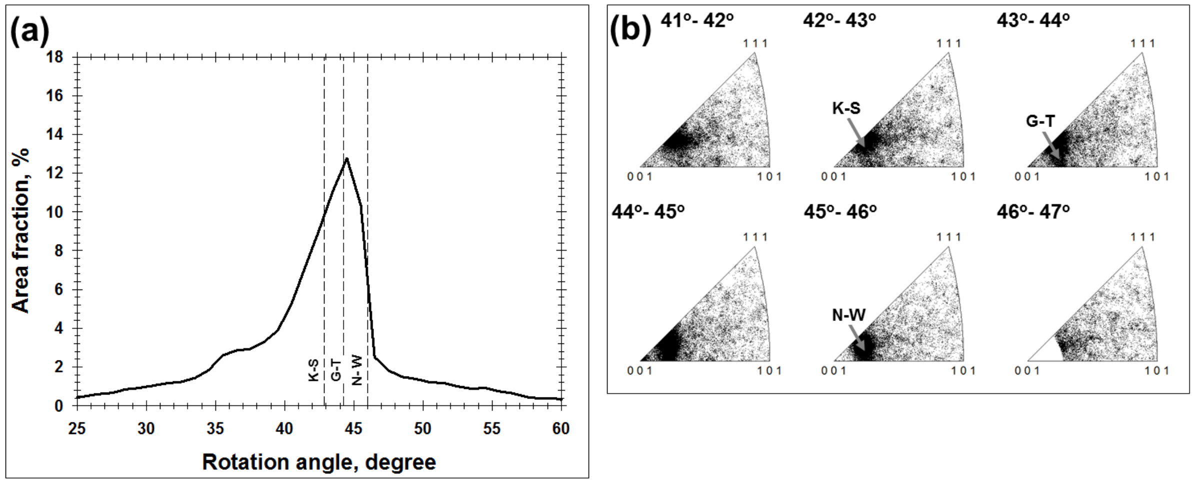

Fig. 3. Examination of orientation relationship between δ-ferrite and austenite using misorientations across the phase boundaries:
a – misorientation-angle distribution and b – misorientation-axis distribution.
The dotted lines in (a) and arrows in (b) indicate the approximate positions of the Kurdjumov–Sachs (K-S), Greniger–Trojano (G-T), and Nishiyama–Wasserman (N-W) orientation relationships

Рис. 3. Исследование ориентационного соотношения между δ-ферритом и аустенитом с использованием разориентировок вдоль межфазных границ:
а – распределение углов разориентировки и b – распределение осей разориентировки.
Пунктирные линии на (*a*) и стрелки на (*b*) указывают на приблизительные положения ориентационных соотношений Курдюмова–Закса (К-З), Гренингера–Трояно (Г-Т) и Нишиямы–Вассермана (Н-В)

It is clear that the measured orientation relationships varied in the entire range from the K-S to N-W ones (Fig. 3, *a, b*), and the best fit was obtained with an “intermediate” Greniger–Trojano (G-T) relation (Fig. 3, *a*). In martensitic structures, such a “mixed” orientation relationship is often reported in the scientific literature, being usually attributed to a relatively large orientation spread within the martensitic phase [e.g., 17, 18]. As follows from the present result (i.e., the austenitic structure), this phenomenon may also be a characteristic of the δ→γ transformation.

Selection of crystallographic variants. To provide further insight into this phase transformation, misorientation distribution, which evolved within the austenitic phase, was also examined, as shown in Fig. 4, *a*. It was found that the characteristics of the distribution included a significant proportion of low-angle boundaries as well as a pronounced crystallographic preference of 60° <111> misorientations. Considering the orientation relationship between the austenite and δ-ferrite (Fig. 2 and 3), it is reasonable to suggest that the measured misorientation distribution may originate (at least partially) from the phase transformation. Due to the crystal symmetry of both phases, the multiple austenite variants of the orientation relationship may form within a particular parent δ-ferrite grain. Accordingly, the inter-variant boundaries may contribute to the unusual character of the misorientation distribution.

The inter-variant misorientations are often represented as those between the V1 variant and other variants, as shown in Table 2. Assuming the K-S orientation relationship between the δ-ferrite and austenite, the area fractions of the inter-variant boundaries for both examined materials were determined and summarized in Fig. 4, *b*. Because of crystallographic equivalency of some inter-variant misorientations (including V3/V5, V9/V19, V10/V14, V11/V13, V12/V20, V15/V23, and V18/V22 variant pairs), only 16 independent misorientations were measured, as indicated in Fig. 4, *b*.

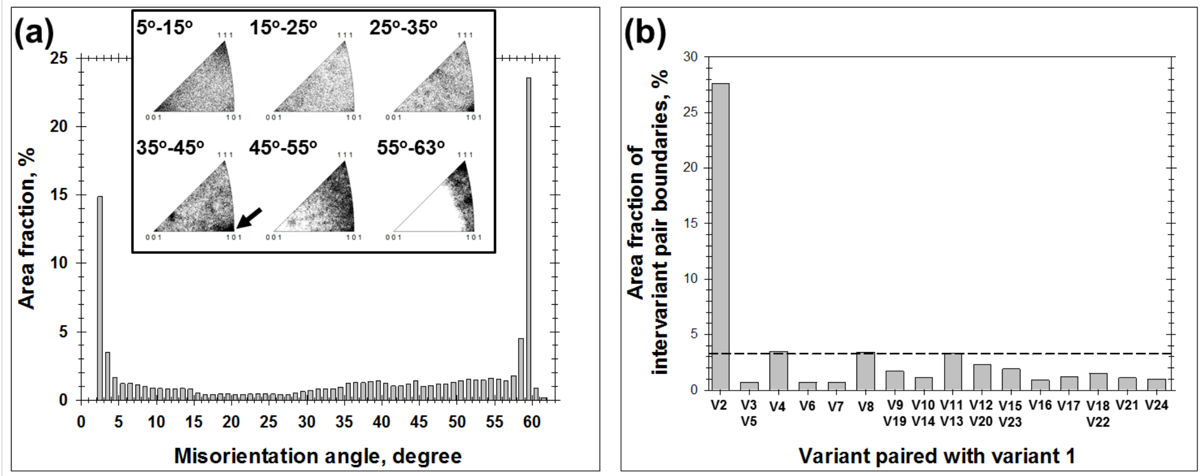

Fig. 4. Misorientation distribution in austenite (*a*) and variant-pairing-frequency histogram (*b*) derived from the austenitic phase assuming the K-S orientation relationship between δ-ferrite and austenite. In (*a*), misorientation-axis distribution is shown as an insert in the top part of the figure; arrow indicate an increased fraction of Σ9 misorientations. In (*b*), the horizontal broken line represents the fraction of inter-variant misorientations assuming no variant selection

Рис. 4. Распределение разориентировок в аустените (*a*) и гистограмма частоты образования пар вариантов (*b*), полученная для аустенитной фазы в предположении ориентационного соотношения К–З между δ-ферритом и аустенитом. На (*a*) распределение осей разориентировки показано в виде вставки в верхней части рисунка; стрелка указывает на повышенную долю разориентировок Σ9. На (*b*) горизонтальная штриховая линия соответствует доле межвариантных разориентировок в предположении отсутствия отбора вариантов

Table 2. Misorientations between austenitic variant V1 and other variants (V2 to V24) for the δ→γ phase transformation assuming the K-S orientation relationship [19]

Таблица 2. Разориентировки между аустенитным вариантом V1 и другими вариантами (V2–V24) для превращения δ→γ в предположении ориентационного соотношения К–З [19]

V2	60°[11-1]	V10	50.5°[-7-5-5]	V18	47.1°[-24;-10;21]
V3	60°[011]	V11	14.9°[13;5;1]	V19	50.5°[-3;13;10]
V4	10.5°[0-1-1]	V12	57.2°[-356]	V20	57.2°[36-5]
V5	60°[0-1-1]	V13	14.9°[5;-13;-1]	V21	20.6°[30-1]
V6	49.5°[011]	V14	50.5°[-55-7]	V22	47.1°[-10;21;24]
V7	49.5°[-1-11]	V15	57.2°[-6-25]	V23	57.2°[-2-5-6]
V8	10.5°[11-1]	V16	20.6°[11;-11;-6]	V24	21.1°[9-40]
V9	50.5°[-10;3;-13]	V17	51.7°[-11;6;-11]		

The measurements revealed a distinct crystallographic preference for V1/V2 inter-variant boundaries (Fig. 4, *b*), i.e., the 60° [11-1] misorientation (Table 2). This finding suggested a strong variant selection during the δ→γ phase transformation. This phenomenon gave rise to a distinct crystallographic preference for the 60° <111> misorientations (Fig. 4, *a*) in the austenitic phase.

The prevalence of the twin-related crystallographic variants during austenite reversion has also been reported by Nakada and colleagues [20]. This effect has been attributed to the significant residual stress in the parent martensitic phase. Given the extremely high cooling rate, which is intrinsic to the L-PBF process, it is highly likely that the δ-ferrite in the present study was also characterized by considerable residual stress. Therefore, the concept proposed by Nakada and colleagues [20] explains well the pronounced variant selection during the δ→γ phase transformation, at least in the present study.

It is also important to emphasize that the misorientation distribution in the austenitic phase exhibited an increased fraction (≈3.0%) of 39° <110> (or Σ9) boundaries (Fig. 4, *a*, arrow in the insert). Those could not be directly associated with the displacive phase transformation mechanism. On the other hand, this finding correlates well with the apparently recrystallized austenite particles revealed in the microstructure (arrow in Fig. 1, *b*). Hence, it is likely that the diffusion-driven mechanisms also contributed to the δ→γ phase transformation.

Summary

1. EBSD analysis revealed a distinct difference between austenite particles in morphology (lath-shaped vs. equiaxed) and density of lattice defects. Moreover, misorientation distribution in the austenitic phase exhibited an increased fraction of both the inter-variant boundaries and Σ9 boundaries. Based on these observations, it was suggested that the δ→γ phase transformation was governed by two different mechanisms, i.e., the displacive and diffusion-driven ones.
2. Statistical analysis showed that the orientation relationship between the δ-ferrite and austenite varied over a wide range between the "classical" K-S and N-W relations. This phenomenon was likely a result of a significant orientation spread within the phases.
3. The δ→γ phase transformation involved a strict selection of crystallographic variants with a distinct preference for the twin-related variants. This effect was explained in terms of high residual stresses within the parent δ-ferrite phase.

Acknowledgments / Благодарности

The work was supported by the government assignment FZWG-2026-0005 "Development of scientific foundations for optimization of selective laser melting and subsequent heat treatment of precipitation-hardening martensitic steel 17-4 PH", Ministry of Science and Higher Education of the Russian Federation. The experimental works were conducted using equipment of the Joint Research Center "Technology and Materials" at Belgorod State National Research University.

Работа выполнена в рамках государственного задания Министерства науки и высшего образования Российской Федерации № FZWG-2026-0005 «Разработка научных основ оптимизации селективного лазерного плавления и последующей термической обработки дисперсионно-твердеющей мартенситной стали 17-4 PH». Экспериментальные исследования проводились на оборудовании Центра коллективного пользования «Технологии и материалы» НИУ «БелГУ».

REFERENCES

1. Ghoncheh M.H., Shahriari A., Birbilis N., Mohammadi M. Process-microstructure-corrosion of additively manufactured steels: a review // Critical Reviews in Solid State and Materials Sciences. 49, 607–717 (2023). https://doi.org/10.1080/10408436.2023.2255616.

2. Zuiko I.S., Dolzhenko P.D., Borisov S.I., et al. Laser powder bed fusion of martensitic precipitation hardenable steep 17-4 PH: A critical review // Physical Mesomechanics. In print.

3. Patra S., Ghosh A., Kumar V., Chakrabarti D., Singhal L.K. Deformation induced austenite formation in as-cast 2101 duplex stainless steel and its effect on hot-ductility // Materials Science and Engineering: A. 660, 61–70 (2016). https://doi.org/10.1016/j.msea.2016.02.067.

4. Vysotskiy I., Malopheyev S., Zuiko I., et al. Crystallographic aspects of 17–4 PH martensitic steel produced by laser-powder bed fusion // Materials Characterization. 194, 112405 (2022). https://doi.org/10.1016/j.matchar.2022.112405.

5. Liu Y., Sun Y. In-situ observation of interaction between precipitates and austenite during δ→γ phase transformations // Materials Science and Technology. 35,

536–543 (2019). https://doi.org/10.1080/02670836.2019.1572299.

6. He X.Y., Xu Z.P., Rohrer G.S., et al. Three-dimensional analysis of the delta-ferrite to austenite phase transformation in an additively manufactured duplex stainless steel // Materials Characterization. 221, 114745 (2025). https://doi.org/10.1016/j.matchar.2025.114745.

7. Dalton J.C., Ernst F., Heuer A.H. Low-temperature nitridation of 2205 duplex stainless steel // Metallurgical and Materials Transactions A. 51, 608–617 (2020). https://doi.org/10.1007/s11661-019-05553-x.

8. Tomida T., Maehara Y., Ohmori Y. Martensitic transformation from d-ferrite during the melt-quenching process of d/g duplex stainless steel // Materials Transactions JIM. 30, 326–336 (1989). https://doi.org/10.2320/matertrans1989.30.326.

9. Haghdadi N., Cizek P., Hodgson P.D., et al. New insights into the interface characteristics of a duplex stainless steel subjected to accelerated ferrite-to-austenite transformation // Journal of Materials Science. 55, 5322–5339 (2020). https://doi.org/10.1007/s10853-020-04358-3.

10. Sasaki S., Katsumura T., Yanagimoto J. Grain refinement technology for duplex stainless steel using rapid cooling immediately before hot working // Journal of Materials Processing Technology. 281, 116614 (2020). https://doi.org/10.1016/j.jmatprotec.2020.116614.

11. Liu G.L., Yang S.W., Han W.T., et al. The simultaneous occurrence of Kurdjumov-Sachs and irrational orientation relationships between delta-ferrite and austenite phase in a 17Cr–5Ni stainless steel // Materials Science and Engineering: A. 798, 140122 (2020). https://doi.org/10.1016/j.msea.2020.140122.

12. Lobanov M.L., Gusev A.A., Lobanova L.A., Yarkov V.Yu. Crystallographic features of shear transformation in martensitic and martensitic–ferritic stainless steels // Physics of Metals and Metallography. 125, 887–894 (2024). https://doi.org/10.1134/S0031918X24600830.

13. Zhong Y., Zheng Z., Li J., Wang C. Effect of in-situ transverse magnetic field on microstructure, mechanical properties and corrosion resistance of the directed energy deposited 316L stainless steel // Additive Manufacturing. 68, 103508 (2023). https://doi.org/10.1016/j.addma.2023.103508.

14. Wilkinson A.J. A new method for determining small misorientations from electron back scatter diffraction patterns // Scripta Materialia. 44, 2379–2385 (2001). https://doi.org/10.1016/S1359-6462(01)00943-5.

15. Sato H., Zaefferer S. A study on the formation mechanisms of butterfly-type Martensite in Fe–30% Ni alloy using EBSD-based orientation microscopy // Acta Materialia. 57, 1931–1937 (2009). https://doi.org/10.1016/j.actamat.2008.12.035.

16. Zaefferer S., Elhami N.N., Konijnenberg P. Electron backscatter diffraction (EBSD) techniques for studying phase transformations in steels / Ed. by E. Pereloma, D.V. Edmonds. Phase Transformations in Steels. Woodhead Publishing, 2012. 2: 557–587. https://doi.org/10.1533/9780857096111.4.557.

17. Shibata A., Morito S., Furuhara T., Maki T. Local orientation change inside lenticular martensite plate in Fe–33Ni alloy // Scripta Materialia. 53, 597–602 (2005). https://doi.org/10.1016/j.scriptamat.2005.04.023.

18. Zisman A.A., Zolotorevsky N.Yu., Petrov S.N., et al. Panoramic crystallographic analysis of structure evolution in low-carbon martensitic steel under tempering // Metal Science and Heat Treatment. 60, 142–149 (2018). doi:10.1007/s11041-018-0252-z.

19. Haghdadi N., Cizek P., Hodgson P.D., et al. Effect of ferrite-to-austenite phase transformation path on the interface crystallographic character distributions in a duplex stainless steel // Acta Materialia. 145, 196–209 (2018). https://doi.org/10.1016/j.actamat.2017.11.057.

20. Nakada N., Tsuchiyama T., Takaki S., Hashizume S. Variant selection of reversed austenite in lath martensite // ISIJ. 47, 1527–1532 (2007). https://doi.org/10.2355/isijinternational.47.1527.